Available online at www.sciencedirect.com
ScienceDirect
Microporous and Mesoporous Materials 98 (2007) 267–282
MICROPOROUS AND MESOPOROUS MATERIALS
www.elsevier.com/locate/micromeso

Structure of the synthetic K-rich phyllomanganate birnessite obtained by high-temperature decomposition of $KMnO_4$ Substructures of K-rich birnessite from 1000 °C experiment

Anne-Claire Gaillot [a], Victor A. Drits [a,b], Alain Manceau [a], Bruno Lanson [a,*]

[a] *Environmental Geochemistry Group, LGIT-Maison des Géosciences, University of Grenoble – CNRS, 38041 Grenoble Cedex 9, France*
[b] *Geological Institute, Russian Academy of Sciences, 7 Pyzhevsky street, 109017 Moscow, Russia*

Received 5 July 2006; received in revised form 25 August 2006; accepted 12 September 2006
Available online 30 October 2006

Abstract

The structure of a synthetic potassium-rich birnessite prepared from the thermal decomposition of $KMnO_4$ at 1000 °C in air has been refined by Rietveld analysis of the powder X-ray diffraction (XRD) data, and the structure model shown to be consistent with extended X-ray absorption fine structure data. K-rich birnessite structure is a two-layer orthorhombic polytype (2O) with unit-cell parameters $a = 5.1554(3)$ Å, $b = 2.8460(1)$ Å, $c = 14.088(1)$ Å, $\alpha = \beta = \gamma = 90°$, $a/b = \sqrt{3.281}$, and was refined in the *Ccmm* space group. The structure is characterized by the regular alternation of octahedral layers rotated with respect to each other by 180°. Octahedral layers are essentially devoid of vacant sites, the presence of 0.25 Mn^{3+}_{layer} cations within these layers being the main source of their deficit of charge, which is compensated for by interlayer K^+ cations. Mn^{3+} octahedra, which are distorted by the Jahn–Teller effect, are systematically elongated along the **a** axis (cooperative Jahn–Teller effect) to minimize steric strains, thus yielding an orthogonal layer symmetry. In addition, Mn^{3+} octahedra are segregated in Mn^{3+}-rich rows parallel to the **b** axis that alternate with two Mn^{4+} rows according to the sequence $\cdots$–Mn^{3+}–Mn^{4+}–Mn^{4+}–Mn^{3+}–$\cdots$ along the *a* direction, thus leading to a $A = 3a$ super-periodicity. At 350 °C, the structure partially collapses due to the departure of interlayer H_2O molecules and undergoes a reversible $2O$ to $2H$ phase transition. This transition results from the relaxation of the cooperative Jahn–Teller effect, that is from the random orientation of elongated Mn^{3+} octahedra.

Keywords: Mn oxide; Birnessite; Phyllomanganate; XRD

1. Introduction

Birnessite is a phyllomanganate, that is a manganese oxide containing predominantly Mn^{4+} cations assembled in layers of edge-sharing MnO_6 octahedra. A layer charge deficit arises from the presence within layers of Mn^{3+} cations and/or vacant layer octahedra and is compensated for by the presence of interlayer cations which are typically hydrolysable cations [1–8]. As such phyllomanganates are very similar to expandable 2:1 phyllosilicates (smectites) and can be considered as $(2 \times \infty)$ microporous solids [9,10]. As smectites, phyllomanganates can be intercalated with a variety of organic and inorganic compounds to form multilayer nanocomposites [11–17], or pillared structures [18–24]. In addition, phyllomanganates have been widely used as templates for the formation of octahedral molecular sieves with variable tunnel sizes that have demonstrated excellent potential in heterogeneous catalysis, hazardous waste remediation, and rechargeable battery technology [25–42]. More recently, mesoporous hollow shells with birnessite walls have also been synthesized [43].

Besides, birnessites play a pivotal role in the fate of heavy metals and other pollutants in contaminated water systems and soils because they possess unique crystal–chemical characteristics which confer them extensive redox

* Corresponding author. Tel.: +33 476 828 017; fax: +33 476 828 101.
E-mail address: bruno.lanson@obs.ujf-grenoble.fr (B. Lanson).

1387-1811/$ - see front matter © 2006 Elsevier Inc. All rights reserved.
doi:10.1016/j.micromeso.2006.09.010

and sorption properties [3,6,44–49]. A large range of birnessite varieties with different structural and chemical characteristics can be synthesized in the laboratory. Synthetic birnessite can be obtained from the oxidation of Mn^{2+} in highly alkaline medium [1,2,50,51], from the thermal decomposition of MnO-containing mixtures [52], and from the reduction of Mn^{7+} [53–59]. In most cases, syntheses are performed at low temperature to obtain surrogate materials representative of natural specimens [1,2,60,61]. Low-temperature birnessites are usually finely dispersed, and often present a low degree of structural order.

Over the last decade an interest for high temperature birnessite (from 170 °C up to 1000 °C) has emerged as the result of their promising potential as electrodes in secondary lithium batteries [52,56–58,62–65]. Kim et al. showed that birnessites with high structural perfection can be obtained at high temperature, these varieties being more stable than those commonly used in electrochemistry [58]. In particular the transition to a spinel structure was not observed after cell cycling. The protocol is based on the thermal decomposition of $KMnO_4$, large K^+ cations pillaring the synthesis products, thus stabilizing the layered framework. In addition, the production of highly oxidizing species during the decomposition prevents the formation of suboxides. As a result, a new variety of synthetic K-rich birnessites with a two-layer periodicity along the **c** axis was obtained [58]. This variety will be hereafter referred to as KBi. These authors performed experiments from 200–1000 °C, but structural and crystal chemical study was limited to high-temperature varieties. The Rietveld technique was used to determine the crystal structure of KBi obtained at 800 °C. In the refined model adjacent vacancy-free layers are rotated with respect to each other by 180° around the **c** axis, which is perpendicular to the layers, and interlayer K^+ is located in a prism defined by tridentate cavities of adjacent layers [58]. Kim et al also synthesized at 1000 °C, a KBi sample that presents a different chemistry but did not refine its structure [58].

The present article, together with its companion [66], further extends the structural characterization of high-temperature KBi synthesized according to the protocol of Kim et al. [58]. This series of articles was initiated by the structure refinement of a KBi sample obtained at 800 °C from single-crystal and powder X-ray diffraction (XRD) and extended X-ray absorption fine structure (EXAFS) spectroscopy experiments [67]. XRD structure refinement has pointed out several significant differences with the model proposed by Kim et al. [58,67]. First, the cation composition of KBi interlayers is heterogeneous and includes both K^+ and Mn^{3+} cations. Second, layers of KBi synthesized at 800 °C contain significant amount of vacant octahedra (12%) and consist exclusively of Mn^{4+} octahedra because of the layer-to-interlayer migration of Mn^{3+} cations. Third, interlayer K^+ is not located in the prism's center but its site is split into three ones, each of which is shifted toward the nearest prism's face in the interlayer mid plane. The determination of these fine structure details should provide a better understanding of the relationship between KBi structure and its properties. The second paper of this series describes the phase and structural heterogeneities of KBi samples synthesized at 200–1000 °C, together with the factors responsible for these heterogeneities [68]. The present work is devoted to the structural characterization of a homogeneous KBi sample obtained at 1000 °C and of this KBi variety when heated to 350 °C. The present article will focus on the average distribution of layer and interlayer cations within the subcell and on the origin of the layer charge, whereas KBi superstructure and its origin will be discussed in the last part of this series of articles devoted to high-temperature KBi structure [66]. One effective tool to study superstructures is to use, along with XRD, selected area electron diffraction (SAED) [5,6,46,69–71]. However, comparison of XRD and SAED data may appear irrelevant because of the possible modification of interlayer species distribution as the result of dehydration under vacuum [57]. XRD experiments were thus performed under deep vacuum conditions to check the consequences of such dehydration on the layer structure and on the interlayer cation distribution.

2. Experimental section

2.1. Experimental methods

K-rich phyllomanganate birnessite (hereafter referred to as KBi) was prepared by thermal decomposition of fine grained $KMnO_4$ powder (particle size <50 μm) at 1000 °C in air according to the procedure of Kim et al. [58,67]. As for the 800 °C synthesis, structural homogeneity of synthetic products was maximized by using flat crucibles containing a thin layer of $KMnO_4$ powder. KBi samples synthesized at 1000 °C (this study) and 800 °C will be hereafter referred to as KBi_{10} and KBi_8 [67], respectively.

The morphology of KBi_{10} particles was observed on a JEOL JSM 6320 F high-resolution scanning electron microscope equipped with a field emission electron source. No significant difference in size or shape was observed between KBi_8 and KBi_{10} crystals, and KBi_{10} particles consist of large micro-crystals with well-defined crystallographic faces [67].

2.2. Thermal and chemical analyses

Thermal analyses were carried out with a NETZSCH Simultan STA 409 EP analyzer. DT–TG data were recorded in air using a 6 °C/min heating rate over the 20–1100 °C temperature range to determine the amount of structural water. Total K and Mn contents were determined using a Perkin–Elmer Optima 3000 ICP–AES after digestion of about 8 mg of KBi powder in 200 mL of 1% HNO_3/0.1% NH_3OHCl matrix. The mean oxidation degree of manganese in birnessite was determined by potentiometric titration using $(NH_4)_2Fe(SO_4)$ Mohr salt and $Na_4P_2O_7$ [72,73]. The mean oxidation state, $2x$, in combination with

the atomic ratio $y = K/Mn$ determined from the chemical analyses, allows calculating the structural formula of KBi using the relation [67]:

$$K^{+}_{2y/w}(Mn^{4+}_{(4x-6)/w}Mn^{3+}_{(8-4x)/w}\square_{1-2/w})O_2 \quad (1)$$

where $w = \frac{2x+y}{2}$, $\square$ represents vacant layer sites. This structural formula can be refined by taking into account the amount of interlayer H_2O molecules ($H_2O_{interlayer}$) deduced from the DT–TG curves.

2.3. X-ray diffraction data collection

Powder XRD patterns were recorded using a Bruker D5000 powder diffractometer equipped with a Kevex Si(Li) solid detector and CuKα_{1+2} radiation. Intensities were recorded from 5 to 90° with a 0.04° 2θ interval, using a 40 sec counting time per step. A rotating sample holder was used for room temperature measurements to minimize the effect of preferential orientation. A Anton Paar TTK450 chamber was used to record XRD patterns from samples heated *in situ*. XRD patterns of KBi_{10} obtained at 100 °C, 150 °C, 250 °C and 350 °C will be hereafter referred to as 100-KBi_{10}, 150-KBi_{10}, 250-KBi_{10} and 350-KBi_{10}, respectively, while the notations KBi_{10} and AfterT-KBi_{10} will be used to differentiate XRD patterns recorded at room-temperature before and after temperature experiments, respectively. All heated KBi diffractograms were recorded successively in a single experiment. The sample was heated *in situ* at a 6 °C/min rate until the target temperature was reached and maintained at a temperature plateau for 2 h before collecting the diffractogram using the same conditions than at room temperature. After ~24 h of data collection, temperature was further increased to the next 2 h plateau. XRD data were finally collected again after cooling the sample back to room temperature (sample AfterT-KBi_{10}). Finally, the same Anton Paar TTK450 chamber allowed studying the structure of KBi_{10} under deep vacuum conditions using a Varian V70 turbo-molecular pump connected to the sample chamber to reach $\sim 10^{-5}$ hPa. After waiting for 15 h to ensure a complete dehydration of the sample, XRD data were collected using the same experimental conditions. This sample will be referred to as Vacuum-KBi_{10}, while the XRD pattern recorded once back at the atmospheric pressure to allow rehydration of this sample will be referred to as After-Vac-KBi_{10}. Note that indexing was performed systematically assuming an orthorhombic *C*-centered unit cell whatever the actual layer symmetry (orthogonal or hexagonal).

2.4. Simulation of powder XRD patterns

The Rietveld technique was used to refine the structure of sample KBi_{10} using the XND code [74]. To de-correlate instrumental broadening, profile shape function (PSF) parameters and spectral distribution were refined first using a reference quartz powder sample [8]. During the subsequent structure refinement process these instrumental parameters were not further refined. A spline function was used to interpolate a background defined by 6–to–8 points. Scale factor and unit-cell parameters were refined first before site coordinates and occupancies. Atomic thermal motion was modeled using isotropic Debye–Waller factors (B). In the final stage of the refinement, orientation parameters were introduced using first degree spherical functions. Fit quality was estimated with the standard R_{wp} and R_B factors. More details on the XND code can be found at <http://www.ccp14.ac.uk/ccp/ccp14/ftp-mirror/xnd/pub/xnd/html/xnd.html>.

2.5. EXAFS experiments

Mn EXAFS spectra were recorded on beamline 10.3.2 at the Advanced Light Source (ALS) of the Lawrence Berkeley National Laboratory (USA). Experimental conditions and data analysis were the same as those reported for KBi_8 [67]. The EXAFS spectra were apodized by a Kaiser–Bessel function ($\beta = 2.5$) and then Fourier transformed to real space to generate radial structure functions (RSFs). RSFs were not corrected for phase shifts, causing peaks to appear at shorter distances ($R + \Delta$, with $\Delta \approx -0.4$ Å) relative to the true interatomic distances (R). Structural parameters from the nearest oxygen and manganese shells (Mn–O and Mn–Mn atomic pairs) were determined by back-transforming to k space the first two RSF peaks, and fitting the data with phase shift and amplitude functions calculated by FEFF7 using λ–MnO_2 as structure model [75,76]. The short-distance Mn–O and Mn–Mn contributions were fitted together because of incomplete separation in the Fourier-filtering process.

3. Results

3.1. Chemical analyses and structural formulae

3.1.1. Amount of interlayer water

The DTA curve of KBi_{10} contains two endotherms at 178 °C and 926 °C, respectively (Fig. 1). The low-temperature endotherm (178 °C) corresponds to the loss of weight

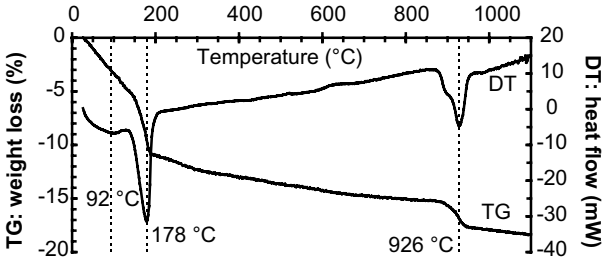

Fig. 1. Experimental TG and DT traces obtained for untreated sample KBi_{10}. Analytical conditions are given in the text.

due to interlayer water, whose amount equals 7.5 wt% (between 120 °C and 210 °C) while the high-temperature endotherm (926 °C) is likely related to KBi melting. The additional loss of weight within the 60 °C–120 °C range is most likely related to water adsorbed on grain surfaces. In contrast to what was observed for sample KBi_8 and hydrothermal birnessite [67,77], no DT peak or change of slope in TG curve was observed over the 250–400 °C interval.

3.1.2. Structural formula

The K/Mn atomic ratio [$y = 0.320(5)$] was calculated from K and Mn ICP concentration values measured from the same solution whereas the H_2O/Mn mole ratio (0.50) was deduced from the weight loss measured between 120 °C and 210 °C and corresponding to the loss of interlayer water. Chemical analyses have shown that the mean oxidation degree was equal to 3.75(2). Using these values and Eq. 1 the following structural formula, in which □ correspond to vacant layer sites, can be deduced for KBi_{10} crystals at room temperature and pressure:

$$K^{+}_{0.314}(Mn^{3+}_{0.246}Mn^{4+}_{0.737\square 0.017})O_2 \cdot 0.50H_2O \quad (2)$$

3.2. Indexing of the experimental XRD patterns

3.2.1. Sample KBi_{10}

The powder XRD pattern (Fig. 2A) contains a rational series of basal reflections with $d(00l)$ values corresponding to a minimum periodicity along the $\mathbf{c}^*$ axis equal to 7.044 Å. The non-basal reflections are intense and sharp. The positions of hkl reflections are compatible with an orthorhombic two-layer ($2O$) C-centered cell with $a = 5.1554(3)$ Å, $b = 2.8460(1)$ Å, $c = 14.088(1)$ Å, $\alpha = \beta = \gamma = 90°$, $a/b = \sqrt{3}.281$ (Table 1). With such an indexing, XRD patterns of birnessites contain $20l/11l$ reflections over the 34–64° 2θ CuKα angular range, $31l/02l$ maxima being visible over the 64–74° 2θ CuKα range and $40l/22l$ over the 74–90° 2θ range. Along with the described hkl reflections, the XRD pattern contains additional weaker reflections, mainly over the 5–34° 2θ region (inset on Fig. 2A), which can be indexed using a C-centered supercell with $A = 3a$, $B = b$, $C = c$, $\alpha = \beta = \gamma = 90°$. This superstructure will be described and its origin discussed in the final part of this four paper series [66].

3.2.2. Sample 100-KBi_{10}

The XRD pattern of 100-KBi_{10} (Fig. 2B) is very similar to that of KBi_{10} and can be indexed with a $2O$ unit cell (Table 1). Previously described super-reflections are still visible.

3.2.3. Sample 150-KBi_{10}

Although TD–TG curves indicate that KBi_{10} dehydrates essentially at ~180 °C, the XRD pattern of 150-KBi_{10} (Fig. 2C) shows a significant decrease of the $d(002)$ value at ~6.44 Å, and related shifts of hkl reflections. The higher temperature deduced from TD–TG curves for the departure of interlayer H_2O molecules likely results from the high heating rate used for the thermal analysis, whereas the 2 h plateau at 150 °C likely allowed reaching complete dehydration before XRD data collection. Apart from the reduction of the unit-cell dimension along the $\mathbf{c}^*$ axis, the birnessite layer structure remains essentially stable, the main reflections being indexed with a $2O$ unit cell (Table 1). A close look at the experimental XRD pattern reveals however that the profile of intense non-basal reflections is altered with shoulders visible on their low-angle sides (shown for the 114 reflection on the inset – Fig. 2C). These additional maxima can be indexed using a two-layer hexagonal ($2H$) unit cell with $a = 5.010(3)$ Å, $b = 2.891(1)$ Å, $c = 12.871(4)$ Å, $\alpha = \beta = \gamma = 90°$, $a/b = \sqrt{3}.00$ (Table 1). Additional low-intensity peaks visible over the 5-30° 2θ range can be indexed using a C-centered supercell with $A = 3a$, $B = 3b$, $C = c$, $\alpha = \beta = \gamma = 90°$.

3.2.4. Samples 250-KBi_{10} and 350-KBi_{10}

At 250 °C dehydration is complete and heating of KBi_{10} at this temperature dramatically modifies the experimental XRD pattern as the result of important structural changes that persist at least up to 350 °C, XRD patterns of both 350-KBi_{10} and 250-KBi_{10} being similar (Fig. 2D-E). The two patterns contain two basal reflections characteristic of birnessite together with a set of intense and sharp non-basal reflections showing that the structural perfection is preserved. However, the orthogonal symmetry of the low-temperature KBi_{10} layers is transformed into a hexagonal one for samples 250-KBi_{10} and 350-KBi_{10}, hkl reflections being then indexed using a two-layer hexagonal unit cell ($2H$ – Table 1). XRD patterns of samples 250-KBi_{10} and 350-KBi_{10} also contain weak super-reflections in the 5–35° 2θ range that are similar to those observed at 150 °C and indexed using a C-centered $A = 3a$, $B = 3b$, $C = c$, $\alpha = \beta = \gamma = 90°$ supercell.

3.2.5. Sample AfterT-KBi_{10}

Reflections present in the experimental XRD patterns of KBi_{10} specimens recorded at room temperature before and after heating at 350 °C (Figs. 2A and F, respectively) have similar positions and intensities. This means that the structural modification undergone during the heating at 350 °C is essentially reversible. The increase of the minimum periodicity along the $\mathbf{c}^*$ axis from 6.42 Å back to 7.02 Å after cooling of the sample shows that birnessite layers rehydrate. The orthogonal layer symmetry is also recovered, reflections of sample AfterT-KBi_{10} being indexed with a two-layer orthorhombic unit cell ($2O$ – Table 1). Super-reflections corresponding to the initial $A = 3a$, $B = b$, $C = c$, $\alpha = \beta = \gamma = 90°$ C-centered supercell are also recovered. However, differences are visible between KBi_{10} and AfterT-KBi_{10} patterns. In particular, in the latter pattern $20l$ reflections are broader and their intensity relative to the $11l$ reflections (with the same l index) significantly dropped as compared to sample KBi_{10} (Figs. 2A,F and

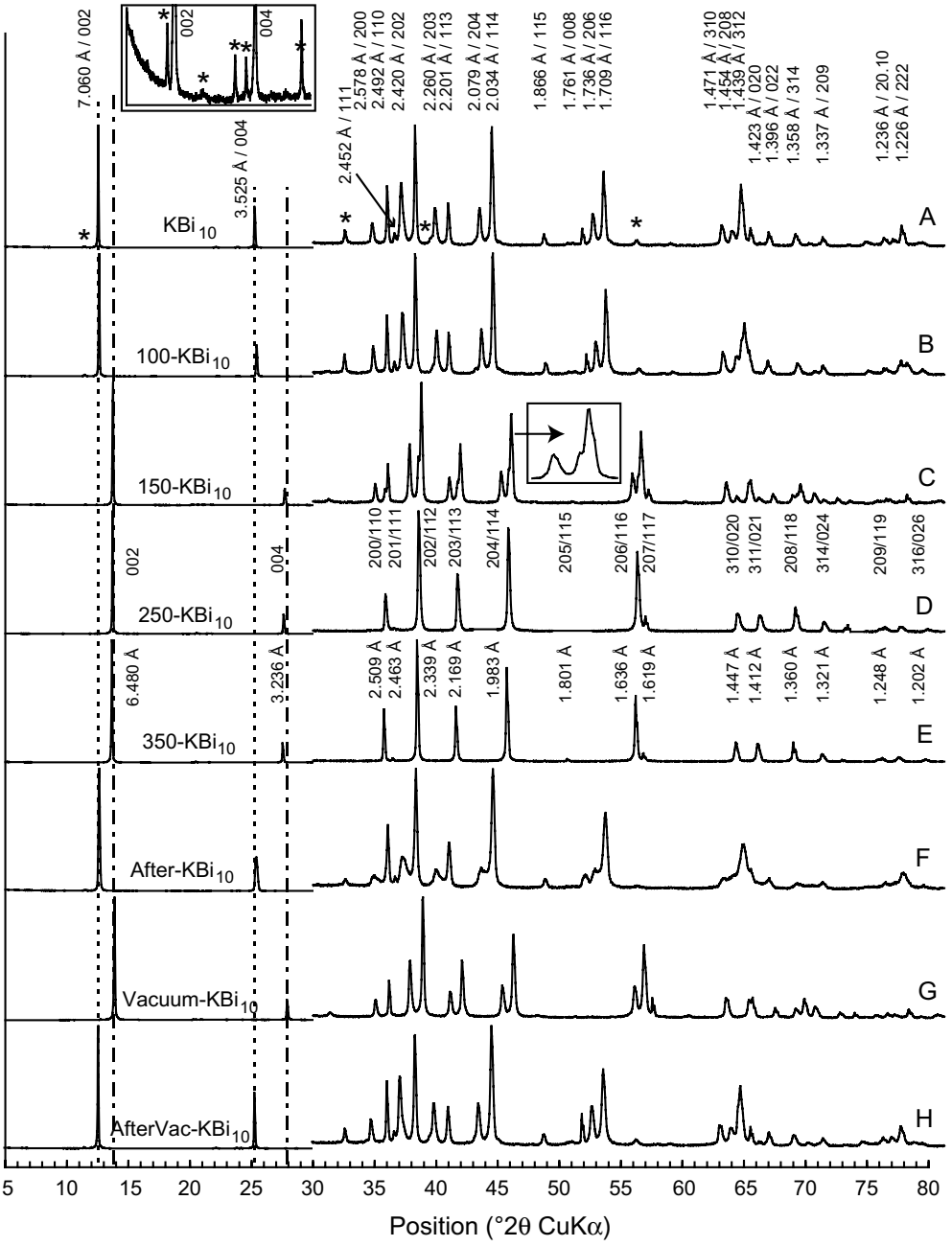

Fig. 2. Experimental powder XRD patterns obtained for KBi_{10} samples. (A) Pattern recorded at room temperature (KBi_{10}). (B)–(E) Patterns recorded *in situ* at successively 100 °C, 150 °C, 250 °C and 350 °C (samples 100-KBi_{10}, 150-KBi_{10}, 250-KBi_{10}, 350-KBi_{10}, respectively). (F) Pattern recorded after complete thermal treatment to 350 °C and subsequent cooling to room temperature (sample AfterT-KBi_{10}). (G) Pattern recorded under vacuum condition (sample Vacuum-KBi_{10}). (H) Pattern recorded after the sample was brought back to atmospheric pressure (sample AfterVac-KBi_{10}). Dotted and dot-dashed lines indicate the position of 00*l* reflections for hydrated and dehydrated samples, respectively. Intensity scale is enlarged over the 30–80° 2θ CuKα angular range, by 9×, 18×, 14×, 13×, 7×, 10×, 14× and 17×, for XRD patterns shown in (A)–(G), respectively. Reflections are indexed using orthorhombic C-centered 2*O* (A–C, F–G) or 2*H* (D–E) unit cells (see supplementary material). Super-reflections are indicated by star symbols.

3). This effect was described in details by Gaillot et al. for the heterogeneous KBi_{10h} variety obtained at 1000 °C [68]. It was shown that 20*l* reflection broadening and weakening are linked to the coexistence of several populations of KBi particles. All populations are 2*O* modifications with slightly different *a* and *b* parameters that are related by the equation:

$$\frac{1}{d(110)^2} = \frac{1}{a_i^2} + \frac{1}{b_i^2} \tag{3}$$

As a consequence, positions of 11*l* reflections are insensitive to the variation of unit-cell parameters, whereas 20*l* reflections of individual 2*O* modifications are slightly shifted. The resulting overlap of 20*l* reflections from

Table 1
Unit-cell parameters of KBi_{10} samples

	a[a]	b	c	a/b	Polytype[b]
KBi_{10}	5.1554(3)	2.8460(1)	14.088(1)	1.811	2*O*
100-KBi_{10}	5.141(1)	2.850(0)	14.002(2)	1.804	2*O*
150-KBi_{10}	5.117(1)	2.845(0)	12.860(2)	1.798	2*O*
150-KBi_{10}	5.010(3)	2.891(1)	12.871(4)	1.733	2*H*
350-KBi_{10}	5.010(2)	2.894(1)	12.954(7)	1.731	2*H*
AfterT-KBi_{10}	5.149(3)	2.846(1)	14.042(7)	1.809	2*O*
Vacuum-KBi_{10}	5.114(2)	2.840(1)	12.787(3)	1.801	2*O*
AfterVac-KBi_{10}	5.160(2)	2.844(1)	14.072(5)	1.815	2*O*

[a] All parameters are expressed in Å. $\alpha = \beta = \gamma = 90°$.
[b] Indexations for 2*O* and 2*H* polytypes are given as supplementary material.

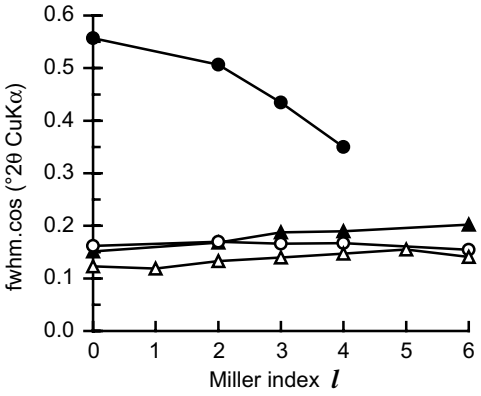

Fig. 3. Evolution of the full width at half-maximum intensity (fwhm) of 20*l* and 11*l* reflections (circles and triangles, respectively) as a function of the Miller index *l* for samples KBi_{10} (open symbols) and AfterT-KBi_{10} (solid symbols). Experimental fwhm values are corrected by a cosθ factor to account for crystal-size broadening [78].

different 2*O* modifications broadens the resulting diffraction maxima, peak broadening decreasing with increasing *l* values (solid circles, Fig. 3).

3.2.6. Sample vacuum-KBi_{10}

The XRD pattern of Vacuum-KBi_{10} is very similar to that of 150-KBi_{10} and presents a shift of basal reflections from 7.044 Å down to 6.397 Å, suggesting the departure of $H_2O_{interlayer}$ (Fig. 2G). As for 150-KBi_{10}, *hkl* reflections are similar to those of KBi_{10} but shifted towards higher angles. In contrast to sample 150-KBi_{10}, no reflections corresponding to a 2*H* modification are visible, all reflections being indexed with a unique 2*O* unit cell (Table 1). Additional weak reflections correspond to a C-centered supercell with $A = 3a$, $B = 3b$, $C = c$, $\alpha = \beta = \gamma = 90°$. Finally, two additional very weak maxima at 6.964 Å and 3.486 Å likely correspond to basal reflections corresponding to a few partially hydrated crystals.

3.2.7. AfterVac-KBi_{10}

The XRD pattern is very similar to that of KBi_{10} with the 002 basal reflection shifted back from 6.397 Å to 7.038 Å indicating the reversibility of the dehydration process. Reflections are indexed using a 2*O* unit cell with parameters very similar to those obtained before dehydration (Table 1). Visible super-reflections correspond to the initial C-centered supercell with $A = 3a$, $B = b$, $C = c$, $\alpha = \beta = \gamma = 90°$.

Unit-cell parameters for all KBi_{10} samples can be found in Table 1, indexation of experimental diffraction lines being provided as supplementary material.

3.3. Structure refinement of KBi_{10} subcells

3.3.1. Rietveld refinement of KBi_{10} subcell

On KBi_{10} XRD pattern all *hkl* reflections consistently have low full width at half maximum intensity (fwhm). In particular, after correction for crystal-size broadening by a cosθ factor [78], fwhm of 11*l* reflections only slightly increases with increasing *l* values (from 0.125° to 0.165° 2θ – open triangles, Fig. 3) whereas that of 20*l* reflections is independent of *l* (0.165° 2θ – open circles, Fig. 3). This data indicates the high structural perfection of KBi_{10}. Small angular regions containing weak super-reflections (at ~37.5°, ~39.5° and ~51.0° 2θ) were excluded from the Rietveld refinement. Atomic positions of KBi_{10} subcell were refined using space group *Ccmm*. Initial occupancies of structural sites correspond to the structural formula of KBi_{10} (Eq. 2). In the initial model schematized on Fig. 4A Mn_{layer} are located at the subcell origin, and O_{layer} have coordinates (0.333, 0, 0.071) to match the ~2.00 Å layer thickness previously refined for several synthetic birnessite structures [5,8,58,67,77,79]. K^+ are located in the interlayer mid-plane, above and below the layer empty tridentate cavities, sharing three edges with octahedra of adjacent layers (TE sites – Fig. 4A), whereas $H_2O_{interlayer}$ are located in-between the nearest O_{layer} from adjacent layers. At this stage $R_{wp} = 22.65\%$ and $R_B = 23.45\%$. All structural parameters were then successively refined, starting from unit-cell parameters, PSFs (the width of basal reflections 00*l* and non-basal *hkl* reflections being described by two sets of parameters) and preferential orientation. Atomic positions and occupancies were then refined. As compared to the initial structure model O_{layer} and $H_2O_{interlayer}$ were shifted along the **a** axis from the initial positions. In addition, the K site was split between three positions located within the interlayer prismatic cavity ($R_{wp} = 12.52\%$, $R_B = 9.57\%$). At this stage, calculated 20*l* and 11*l* reflections are slightly more and less intense, respectively, than corresponding experimental reflections. As 20*l* fwhm values are slightly higher than those of 11*l* ones (solid circles and solid triangles, respectively – Fig. 3A) some KBi_{10} particles likely have unit-cell parameters differing from those of the major part of the sample, unit-cell parameters from the different populations following Eq. 3.

To better fit the broader 20*l* reflections, two PSFs were thus considered for 20*l*/31*l*/40*l* and 11*l*/02*l*/22*l* diffraction lines, respectively, and structural parameters were refined again. The use of two PSFs allowed fitting better the width of all *hkl* reflections, but did not affect signifi-

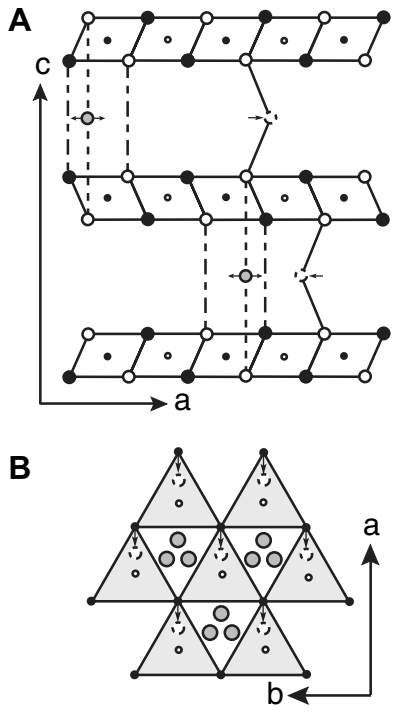

Fig. 4. Structure model for KBi_{10}. (A) Projection along the **b** axis. Open and solid symbols indicate atoms at $y = 0$ and $y = \pm 1/2$, respectively. Large circles represent O_{layer} atoms, small circles represent Mn_{layer} atoms, shaded circles represent $K_{interlayer}$ and open circles with dashed outline represent $H_2O_{interlayer}$. Dot-dashed lines outline the interlayer prisms defined by two empty tridentate layer cavities. The center of these prisms is shown by regular dashed lines, and the arrows outline the shift of K^+ cations from this ideal position. Solid lines represent H-bonds between O_{layer} and $H_2O_{interlayer}$, and the arrows outline the shift of H_2O along the **a** axis from the edge of interlayer prisms. (B) Projection on the **ab** plane. The upper surface of the lower layer is shown as light shaded triangles. O_{layer} and Mn_{layer} atoms of this lower layer are shown as small solid and open circles, respectively. Large shaded circles represent interlayer potassium, and open circles with dashed outline represent water molecules. The arrows outline the shift of H_2O along the **a** axis.

cantly the details of the optimum structure model, whose main parameters are listed in Table 2. The refined site atomic coordinates and occupancies given in Table 3 led to the optimum fit shown in Fig. 5A ($R_{wp} = 11.21\%$, $R_B = 5.50\%$ – Table 2). Selected interatomic distances are listed in Table 4. Consistently with the calculated structural formula (Eq. 1), KBi_{10} consists of vacancy-free layers, the refined Mn_{layer} occupancy being very close to 1.0 (0.985). Deviation of layer symmetry from the hexagonal one induces a significant shift of O_{layer} from the ideal anion close-packing sites [(0.342, 0, 0.070) – Table 3]. This position is similar to that of O_{layer} in Mn^{3+}-bearing birnessite varieties exhibiting an orthogonal layer symmetry [5,8,70]. The refined K^+ site is split into three ones each being shifted in the **ab** plane from the center of the interlayer prism towards its faces [(−0.253, 0, 0.25) and (−0.134, ±0.375, 0.25) – Fig. 4C, Table 3]. Similar positions were obtained if K^+ was initially located at the center of prism faces. Similar K^+ positions were found for KBi_8 and hydrothermal KBi [67,77]. $H_2O_{interlayer}$ are also slightly shifted in the **ab** plane from their initial positions to form a 132.9(3)° angle with the two nearest O_{layer} from adjacent layers [(0.127, 0, 0.25) – Figs. 4C and D]. All attempts to split the $H_2O_{interlayer}$ site from the edge of the prismatic cavity along [1 0 0], [1 1 0] and [1 $\bar{1}$ 0] failed, the site along the *a* direction being systematically the sole with a final significant occupancy.

Table 2
Crystal data and structure refinement for the KBi_{10} sample

Ideal formula	$K^+_{0.314}(Mn^{3+}_{0.246}Mn^{4+}_{0.739\square 0.015})O_2 \cdot 0.50H_2O$
Wavelength	1.54056 Å + 1.54439 Å (Rel. Int. 0.476)
Space group	*Ccmm*
Unit-cell dimensions	$a = 5.1554(3)$ Å
	$b = 2.8460(1)$ Å
	$c = 14.088(1)$ Å
	$V = 206.70$ Å^3
Angular range	34–90°
Data/Parameters	1319/13
Number of reflections	100
R_{Exp}	3.5%
R_{wp}	11.21%
R_{Bragg}	5.50%
Goodness of fit	3.16

3.3.2. Rietveld refinement of 350-KBi_{10} subcell

The initial model was deduced from the refined KBi_{10} model, but 350-KBi_{10} layers were considered to have a hexagonal symmetry, the structure being described in the $P6_3/mmc$ space group. O_{layer} was first assumed to be located in (1/3, 0, 0.078), K^+ positions and occupancies were kept as in KBi_{10}, and no $H_2O_{interlayer}$ was introduced according to TD–TG results. Structural parameters leading to the best fit between experimental and calculated XRD patterns (Fig. 5B – $R_{wp} = 16.80\%$, $R_B = 13.22\%$) are given in Table 3 whereas selected interatomic distances are listed in Table 4. As for KBi_{10}, 350-KBi_{10} layers are essentially devoid of vacancies as the occupancy refined for Mn_{layer} is close to 1.0 (0.983), in agreement with the structural formula proposed for KBi_{10} (Eq. 2). Due to the hexagonal layer symmetry O_{layer} are no longer shifted from the ideal anion close-packing sites [(0.333, 0, 0.079) – Table 3]. Note however that this position was highly unstable when refined. As discussed below this instability may arise from the presence in the layers of Mn^{3+}-octahedra with their long Mn^{3+}-O bonds randomly oriented with respect to the **a** axis. As for KBi_{10} at room temperature, the refined K^+ site is split into three positions, equivalent to (−0.300, 0, 0.25), shifted in the **ab** plane from the prism's center toward one of its faces. Compared to KBi_{10} structure this position is closer to the prism's center likely to provide reasonable K-O_{layer} distances (2.73 Å vs. 2.97 Å, for 350-KBi_{10} and KBi_{10}, respectively) despite the interlayer collapse [77].

3.3.3. Structure of heated KBi_{10} samples

Between 100 °C and 150 °C a 2*O*–to–2*H* structural transformation occurs as described in the indexation

Table 3
Atomic positions and site occupancies for KBi_{10} 2*O*, vacuum-KBi 2*O* and 350-KBi_{10} 2*H* samples

	KBi_{10}				Vacuum-KBi_{10}				350-KBi10			
	x[a]	y	z	Occ.	x	y	z	Occ.	x	y	z	Occ.
Mn_{layer}	0	0	0	0.985(6)	0	0	0	0.983	0	0	0	0.983
O_{layer}	0.342(1)	0	0.0700(6)	2.000	0.341	0	0.0762	2.000	0.333	0	0.0788	2.000
K	−0.253(24)	0	1/4	0.077(28)	−0.300	0	1/4	0.121	−0.300	0	1/4	0.104
K	0.134(8)	±0.375(23)	1/4	0.235(28)	0.153	±0.459	1/4	0.191	0.150	±0.450	1/4	0.208
H_2O	0.127(5)	0	1/4	0.500								

[a] Atomic positions are given according to orthogonal axes, even for 2*H* 350-KBi_{10}. The values of Debye-Waller factors (B) are 0.5, 1.0, 2.0, 2.0 for Mn_{layer}, O_{layer}, K and H_2O, respectively.

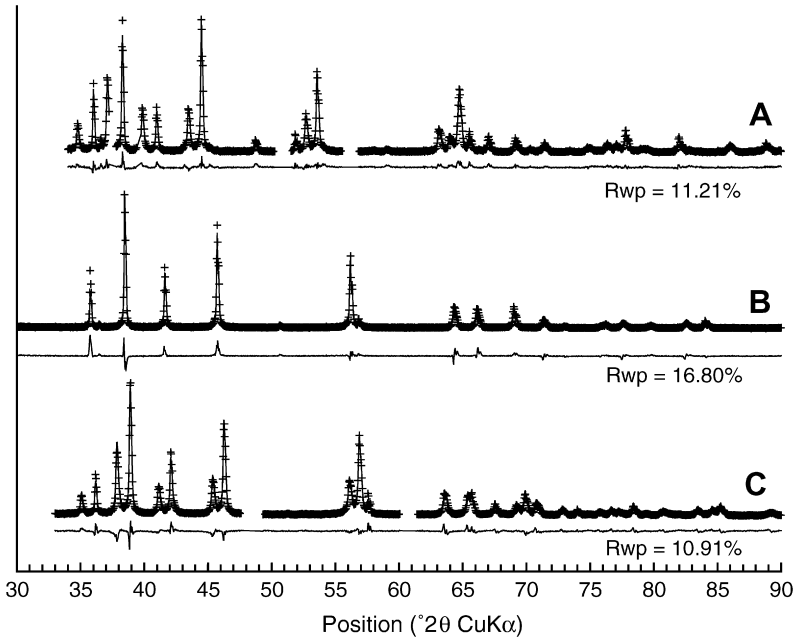

Fig. 5. Comparison between experimental (crosses) and calculated (solid line) XRD patterns for KBi_{10} samples. (A) Sample KBi_{10}, (B) sample 350-KBi_{10} and (C) sample vacuum-KBi_{10}. Atomic coordinates, site occupancies and other structural parameters used for the calculations are listed in Table 3. Difference plot is given for each case. Angular regions with significant contributions from super-reflections were excluded from the fits.

section. The structure of 100-KBi_{10} is assumed to be identical to the 2*O* modification of KBi_{10} whereas 150-KBi_{10} can be considered as a physical mixture of hydrated 2*O* and dehydrated 2*H* structures (similar to samples KBi_{10} and 350-KBi_{10}, respectively). At 250 °C, dehydration and 2*O*–to–2*H* structural changes are complete, and the structure of sample 250-KBi_{10} was assumed to be identical to that of 350-KBi_{10}. No structural refinement was performed on these three samples.

3.3.4. Rietveld refinement of vacuum-KBi_{10} subcell

As for KBi_{10}, small angular regions containing super-reflections (at ~43.5° and ~52.0° 2θ) were excluded from the refinement. The initial structure model was identical to that of KBi_{10} without $H_2O_{interlayer}$ in agreement with the dehydration under deep vacuum conditions. As for KBi_{10}, two PSFs were used to account for the increased width of 20*l*/31*l*/40*l* diffraction lines compared to 11*l*/02*l*/22*l* ones. The best fit is shown on Fig. 5C ($R_{wp} = 10.91\%$, $R_B = 6.85\%$). Refined O_{layer} positions (0.341, 0, 0.076) are similar to those in the original model, while refined K^+ positions are moved toward the prism's center [(−0.300, 0, 0.25) and (0.153, ±0.459, 0.25)], as found for sample 350-KBi_{10}. Refined structural parameters and selected inter-atomic distances are listed in Tables 3 and 4, respectively.

3.4. Qualitative and quantitative analysis of the EXAFS spectra of KBi_{10} and related synthetic birnessites

The short range order of Mn in KBi_{10} was determined by using synthetic Na- and H-birnessite (hereafter referred to as NaBi and HBi, respectively) as references. The crystal structures of NaBi and HBi were determined by X-ray and electron diffraction and EXAFS spectroscopy [8,46,47,80]. Triclinic NaBi consists of vacancy-free Mn layers and its

Table 4
Selected inter-atomic distances in high-temperature KBi_{10} samples

		KBi_{10}	Vacuum-KBi_{10}	350-KBi_{10}
Height of Mn layer		1.972[a]	1.974	2.015
Mn_{layer}–Mn_{layer}	Short	2.846(0) × 2	2.839 × 2	2.895
	Long	2.944(0) × 4	2.924 × 4	
	Average	2.911	2.896	
Mn_{layer}–O_{layer}	Short	1.914(5) × 4	1.903 × 4	1.958
	Long	2.018(6) × 2	1.998 × 2	
	Average	1.949	1.934	
K–O_{layer}	Short	2.948(28)–2.973(23) × 4	2.735 × 4	2.731 × 4
	Long	3.277(78)–3.287(38) × 2	2.868 × 2	2.880 × 2
	Average	3.061–3.067	2.784	2.808
$K_{interlayer}$–$H_2O_{interlayer}$		3.197(137)– 3.611(49)		
O_{layer}–$H_2O_{interlayer}$		2.767(12)		
O_{layer}–H_2O-O_{layer} angle		132.88(25)°		

[a] All distances in Å.

structural formula is $Na^{+}_{0.31}(Mn^{4+}_{0.69}Mn^{3+}_{0.31})O_2 \cdot 0.40\,H_2O$. Mn^{3+} octahedra, which are elongated by the Jahn–Teller effect, are ordered in rows along [0 1 0] that are separated by two Mn^{4+} rows along [1 0 0]. Due to this cation ordering and the distortion of the Mn^{3+} octahedra, the layer symmetry departs from hexagonal to orthogonal [8,46]. The structural formula of HBi at pH_4 is $H^{+}_{0.33}Mn^{2+}_{0.043}Mn^{3+}_{0.123}(Mn^{4+}_{0.722}Mn^{3+}_{0.111}\square_{0.167})O_2(OH)_{0.013}$, where $\square$ represents vacancies [80]. Its layer contains much less Mn^{3+} than NaBi (13% vs. 31%) and, as a consequence, it has a hexagonal symmetry. HBi structure also differs from that of NaBi by the presence of cationic layer vacancies, which are capped by interlayer Mn^{3+} and Mn^{2+} cations. As a result, NaBi has only edge-sharing Mn_{layer} octahedra whereas HBi contains in addition corner-sharing $Mn_{interlayer}$–Mn_{layer} pairs with a distance separation of about 3.52 Å. Another important distinction between these two references is that the Mn_{layer}–Mn_{layer} EXAFS distances are equal in HBi (2.89 Å) and unequal in NaBi (2.89 and 3.01 Å) [67], owing to the hexagonal vs. orthogonal layer symmetry.

Figs. 6A–B show that the resonance at $k = 8.05$ Å^{-1} in HBi is split in two maxima at 7.8 and 8.1–8.2 Å^{-1} in NaBi and KBi_{10}. Previous studies have shown that this indicator region is sensitive to the amount and ordering of Mn^{3+}_{layer} [67,81–83]. When the layer has no Mn^{3+}, the resonance peaks at 8.05 Å^{-1}. When it contains 1/3 Mn^{3+} and 2/3 Mn^{4+}, and the Mn^{3+} cations are not orderly distributed in rows, as in lithiophorite, then the hexagonal symmetry of the layer is preserved and the resonance is shifted to lower k values (higher interatomic distances), peaking at 7.9 Å^{-1} [83]. In contrast, the resonance is split when the Mn–Mn distances have essentially a bimodal distribution, that is when Mn^{3+}_{layer} are segregated in rows. Using that spectroscopic feature as a structural fingerprint for Mn ordering in phyllomanganates, KBi_{10} and NaBi have the same Mn^{3+}–Mn^{4+} distribution patterns. The absence of interlayer Mn atoms follows also from the comparison of the RSFs for KBi_{10}, NaBi and HBi (Figs. 6C–D). The corner-sharing $Mn_{interlayer}$–Mn_{layer} correlation gives a peak at $R + \Delta = 3.1$ Å [47,84], observed in HBi but neither in NaBi nor in KBi_{10}. Although Mn clearly has a similar environment in KBi_{10} and NaBi, the average bond lengths at the Mn site are not strictly identical. The EXAFS spectrum of KBi_{10} is shifted towards the high k values relative to NaBi (Fig. 6A), and this frequency modification induces a left-shift of the imaginary part of the Mn shells in the real space (Fig. 6E). Comparing the imaginary parts for the three phyllomanganates, we find that the average Mn–Mn distances decreases from NaBi, to KBi_{10}, to HBi (Fig. 6E-F). This trend is consistent with the evolution of the fractional amounts of Mn^{3+}_{layer} in the three compounds: 0.31 in NaBi, 0.25 in KBi_{10}, and 0.13 in HBi. The O shell has lesser sensitivity than the Mn shell to the amount of Mn^{3+}_{layer} because the four equatorial Mn^{3+}–O distances (~1.93 Å) [85], are similar to the Mn^{4+}–O distances (~1.91–1.92 Å) [47,76,86], and because the two distant Mn^{3+}–O pairs at 2.2–2.3 Å make a low contribution to the total EXAFS signal (33% of the Mn–O pairs for 25% of the Mn cations, that is 8% of the total Mn–O pairs) [47]. Still, close examination of Figs. 6E–F shows that the imaginary part of the O shell for KBi_{10} is superimposed to that for HBi, but slightly left-shifted relative to that for NaBi. Consistently, the best-fit Mn–O EXAFS distance for KBi_{10} was equal to 1.91 Å as in HBi, 0.01 Å shorter than in NaBi (Table 5). The similarity of the O shell parameters for KBi_{10} and HBi is explained with reference to the fact that the first RSF peaks are the weighted sum from all the Mn atoms present in the structure. When Mn_{layer} and $Mn_{interlayer}$ atoms in HBi are added, then HBi and KBi_{10} have almost the same Mn^{3+}/Mn_{total} ratio (0.24 vs. 0.25).

Similarly to NaBi, a two-shell fit to the Mn–Mn contribution provided an optimal simulation to the data (Table 5). The short-distance Mn–Mn correlation at 2.89 Å is attributed to the Mn^{4+}–Mn^{4+} and Mn^{3+}–Mn^{3+} pairs, and the long-distance Mn–Mn correlation at ~3.01–3.02 Å to the Mn^{4+}–Mn^{3+} pairs [47]. In NaBi, the first subshell contains about 3.6 atoms and the second about 2.4, while they contain about 3.5 and 1.6 atoms in KBi_{10}, respectively. Although the differences in coordination numbers between the two samples are within accuracy, the apparent decrease of the number of the long-distance pairs in KBi_{10} is consistent with the decrease of its Mn^{3+} content. The fact that the double antinode at ~8 Å^{-1} is less pronounced in KBi_{10} than in NaBi (Fig. 6A) is definite evidence of the attenuation of the Mn shell splitting caused by lower amounts of Mn^{3+}.

Overall, the structure models proposed here for KBi_{10}, and previously for HBi and NaBi [47], are consistent with XRD and EXAFS data. Upon closer examination, however, it appears that EXAFS gives shorter Mn–O and longer Mn–Mn distances than XRD, and that the number

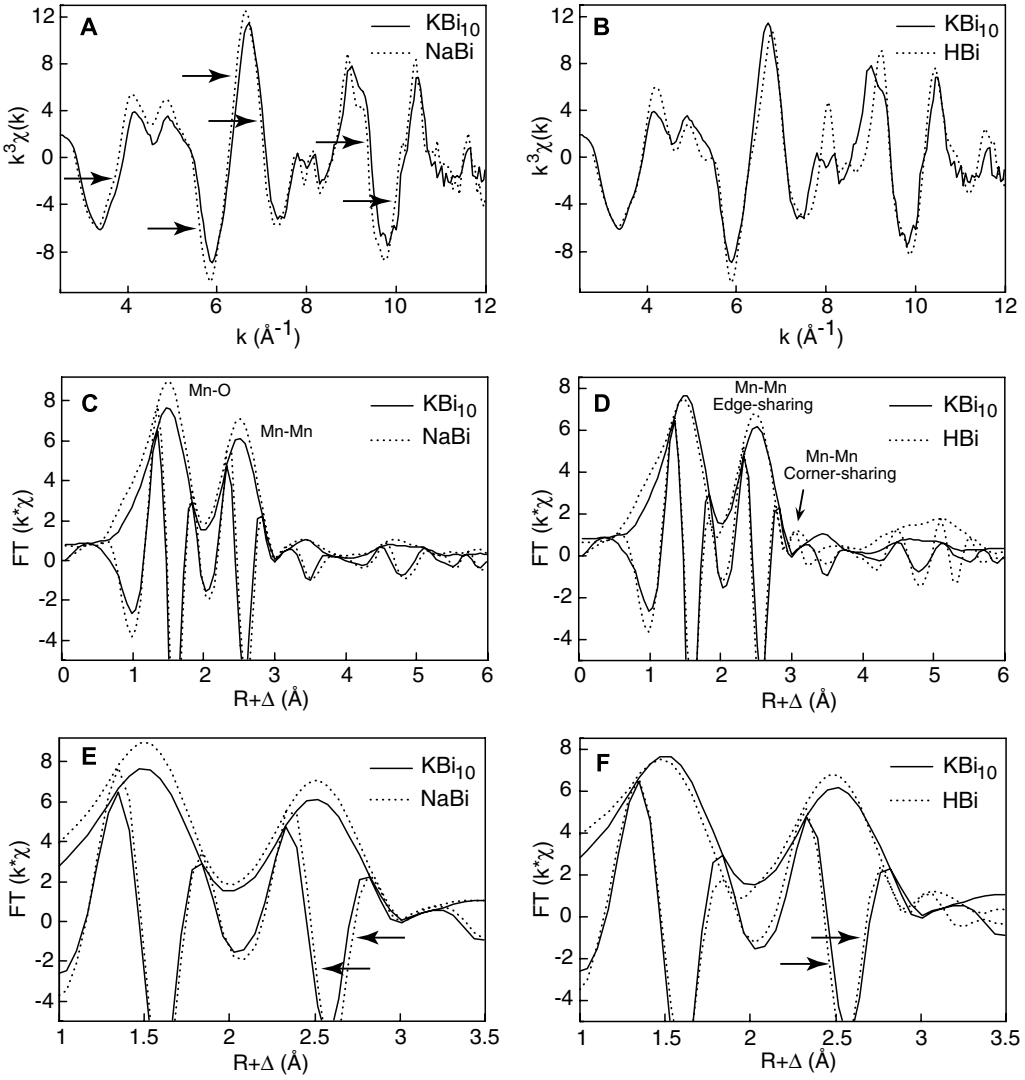

Fig. 6. k^3-weighted EXAFS spectra and Fourier transforms (modulus and imaginary parts) of k-weighted EXAFS spectra for KBi_{10}, triclinic 1T NaBi and hexagonal 1H HBi (pH_4). The EXAFS spectrum of KBi_{10} has the same shape as that of NaBi, but a lower frequency, which manifests itself in a shift to lower distance of the Mn–O and Mn–Mn pairs in the real space.

of oxygens in the first shell often is lower than six (Tables 3–5). The discrepancy between the first shell structural parameters derived by the two techniques has a simple explanation. In Mn^{3+}-containing phyllomanganates, the distribution of Mn–O distances is broad (from ~1.91 Å to 2.2–2.3 Å) and highly asymmetrical due to the elongation of the Mn^{3+} octahedra. When the interlayer contains Mn atoms, as in HBi, the interlayer Mn–O and Mn–H_2O distances are longer than the average Mn–O distance in the layer (Table 6). In these mixed-valency and multi Mn sites compounds, the EXAFS analysis of the O shell with a standard Gaussian-shell model excludes the full distribution of interatomic distances [87]. Since the tail of the distance separation is stretched towards higher R values (e.g., 2.2–2.3 Å for Mn^{3+} and 1.98–2.08 Å for interlayer Mn), analysis of the data using symmetrical distributions leads to lower numbers of O atoms around each Mn atom, and the EXAFS-derived ⟨Mn–O⟩ distance is thus shorter than the weighted average crystallographic value. Cumulant analysis was tested in the present study but proved unsuccessful to detect the "lost" atoms, because the tail apparently does not die off fast enough for cumulants of high orders to be neglected (i.e., the asymmetry is too high).

This complication is circumvented sometimes in the literature by fixing the total number of oxygens (CN) to six in the spectral fits [88,89]. This modelling strategy is inappropriate when the structural disorder is high because the effective number of oxygen atoms detected by EXAFS in the harmonic approximation is lower than six. In a recent study, the O shell of a series of phyllomanganates was fitted with two Gaussian functions centred at 1.85–1.89 Å and 1.90–1.94 Å, and by constraining $CN = 6$ (Table 6) [90]. However, the distance separation between the two functions is not high enough to include the longer bond lengths and the total number of oxygens which can be recovered by

Table 5
EXAFS parameters for the nearest Mn–O and Mn–Mn pairs in birnessite samples and in the reference λ–MnO_2

Sample	$R + \Delta R$ window (Å)	Fit interval ($Å^{-1}$)	Shell	R[a] (Å)	CN[b]	σ^{2}[c] ($Å^2$)	ΔE[d] (eV)	Residual[e]
λ–MnO_2	1.1–3.3	$3.7 < k < 13.5$	Mn–O	1.91	6	25×10^{-4}	1.5	12
			$Mn–Mn_{edge}$	2.85	6	28×10^{-4}		
			Mn–O[f]	3.52	6[g]	88×10^{-4}		
HBi[h]	1.1–3.4	$3.7 < k < 12$	Mn–O	1.91	4.5	32×10^{-4}	1.6	7
			$Mn–Mn_{edge}$	2.89	4.8	51×10^{-4}[i]		
			$Mn–Mn_{corner}$	3.49	2.8	51×10^{-4}[i]		
			Mn–O[f]	3.61	6[g]	49×10^{-4}		
NaBi[h]	1.1–3.7	$3.7 < k < 13.5$	Mn–O	1.92	5.6	30×10^{-4}	0.7	14
			$Mn–Mn_{edge}$	2.89	3.6	40×10^{-4}[i]		
			$Mn–Mn_{edge}$	3.01	2.4	40×10^{-4}[i]		
			Mn–O[f]	3.57	6[g]	12×10^{-3}		
KBi_{10}	1.1–3.7	$3.7 < k < 12$	Mn–O	1.91	4.8	29×10^{-4}	1.3	14
			$Mn–Mn_{edge}$	2.89	3.5	29×10^{-4}[i]		
			$Mn–Mn_{edge}$	3.02	1.6	29×10^{-4}[i]		
			Mn–O[f]	3.58	6[g]	14×10^{-3}		

[a] Accuracy and precision in average distances are ±0.02 and ±0.01 Å, respectively. In λ–MnO_2, the crystallographic Mn–O and Mn–Mn distances are 1.91 Å and 2.84 Å, respectively [76].
[b] Coordination number. The scaling factor S_0^2 was calculated to obtain CN = 6 in the reference λ–MnO_2: $S_0^2 = 0.73$ for the Mn–O pair and 0.80 for the Mn–Mn pair [96]. Typical accuracy on coordination numbers is ±1.5.
[c] Debye–Waller factor.
[d] Variation of the energy threshold treated as a single adjustable parameter for all subshells.
[e] Residual is calculated from $R = [\Sigma|(k^3\chi_{exp} - k^3\chi_{cal})|/\Sigma|k^3\chi_{exp}|] \times 100$.
[f] Second Mn–O shell.
[g] Fixed value in the optimization procedure.
[h] EXAFS results are, within accuracy, identical to those published by Silvester et al. [47].
[i] Parameter varied but constrained equal for the two subshells.

Table 6
EXAFS parameters for the nearest Mn–O and Mn–Mn pairs in birnessite reported by Webb et al. [90]

Sample	Shell	XRD[a]		EXAFS		
		R (Å)	CN[b]	R (Å)	CN	σ^2 ($Å^2$)
NaBi	Mn–O	1.92	2	1.87(2)	4[b]	0.005(2)
		1.94	2	1.94(1)	2[b]	0.002(1)
		2.00	2			
	$Mn–Mn_{edge}$	2.85	2	2.88(3)	2[c]	0.006(1)[d]
		2.95	4	2.90(3)	4[c]	0.006(1)[d]
	$Mn–Mn_{corner}$	–	–	3.36(9)	0.8(8)	0.006(3)
HBi	$Mn_{layer}–O$	1.92	5	1.89(3)	4[c]	0.008(2)
	$Mn_{interlayer}–O$	1.98	0.5	1.90(2)	2[c]	0.004(2)
	$Mn–H_2O$	2.08	0.5			
	$Mn–Mn_{edge}$	2.85	3.5	2.84(1)	2[c]	0.005(1)[d]
				2.89(1)	4[c]	0.005(1)[d]
	$Mn–Mn_{corner}$	3.54	1.8	3.48(1)	2.0(1.1)	0.003(3)

[a] Data from Lanson et al. [8,80].
[b] Theoretical EXAFS CN values calculated from XRD data.
[c] *CN* values were fixed during the fit.
[d] Parameter varied but constrained equal for the two subshells.

this alternative model is thus lower than six. For example, in NaBi, the number of oxygens at short distance is $0.69 \times 6 + 0.31 \times 4 = 5.4$. In this recent study, the analysis of the Mn shell is also problematic for three reasons (Table 6). First, NaBi does not have corner-sharing Mn octahedra. Second, if 0.8 $Mn–Mn_{corner}$ pairs were present in this compound, as assumed from EXAFS, then the number of $Mn–Mn_{edge}$ pairs should be lower than six, since interlayer Mn octahedra do not share edges with other Mn octahedra. The same reasoning applies to HBi. Although this compound actually contains interlayer Mn, the number of $Mn–Mn_{edge}$ pairs was arbitrarily fixed to six by the authors. The average number of $Mn–Mn_{edge}$ pairs in HBi can be calculated from its structure as the weighted sum of the different environments:

$$CN_{edge} = \sum_i W_i CN_i \quad (4)$$

where i refers to Mn site, W_i to Mn site occupancy, and CN_i to the number of Mn neighbors for site i. For HBi, $CN_{edge} = 0.666 \times 4 + 0.166 \times 5 = 3.5$, as there are 50% vacancies in the Mn^{3+}-rich rows, and each Mn in these rows is surrounded by five Mn [47]. Our EXAFS CN value for KBi_{10} (4.8) agrees with theory (3.5) within accuracy, but not the prescribed value of six in the alternative model. Third, the Mn–Mn edge-sharing distances are split in NaBi, due to the orthogonal symmetry of the layer, but not in HBi, whose layer symmetry is hexagonal. From XRD data, the distance separation in NaBi is $2.95 - 2.85 = 0.10$ Å (Table 6). In the alternative EXAFS model, the distance separation in NaBi is as small as $2.90 - 2.88 = 0.02$ Å and, thus, incompatible with the orthogonal layer symmetry. The results reported for HBi are even more questionable: not only the Mn–Mn distances were assumed to be split but, in addition, in an amount ($2.89 - 2.84 = 0.05$ Å) higher than in NaBi.

The Mn–Mn edge-sharing distances obtained here by EXAFS for HBi (2.89 Å) and NaBi (2.89 + 3.01 Å) are ~0.04 Å longer than those obtained by XRD (2.85 Å and 2.85 + 2.95 Å, respectively – Tables 4 and 5). This difference is regarded as significant as EXAFS and XRD give the same Mn–Mn distance in λ–MnO_2. The discrepancy between the lattice parameter values (XRD) and the cation–cation distances (EXAFS) can be reconciled by considering that the octahedral layer is corrugated. In increasing the Mn–Mn distance, the buckling of the octahedral layer minimizes the cationic repulsion and contributes to increase the layer stability. This effect has been described first in hydrotalcite by combining XRD, anomalous scattering and EXAFS spectroscopy [91], and was subsequently inferred to occur also in birnessite from the quantitative analysis of the long distance Mn–Mn–Mn multiple scattering paths in EXAFS [90,92], The angular deviation from the layer planarity, as estimated from the difference of the EXAFS and XRD distances, is $\alpha = \cos^{-1}(2.85/2.89) \sim \cos^{-1}(2.95/3.01) \sim 10.5(10)^\circ$ in HBi and NaBi.

4. Discussion

The structure of high-temperature KBi synthesized at 1000 °C (KBi_{10} – this study) differs substantially from that of KBi obtained at 800 °C (KBi_8), whose structure was described in the first of this four paper series [67]. Differences in chemical composition, layer symmetry and origin of the layer charge between KBi_8 and KBi_{10} are discussed first. Then, the nature of structural modifications induced by thermal treatment at 350 °C of KBi_{10} is examined. From these considerations and the comparison with structural features of other birnessites and layer Mn oxyhydroxides, a generalized relationship between the layer symmetry and the origin of the layer charge is proposed. Finally, the possible modification of the layer and interlayer structure of KBi_{10} in vacuum is discussed, and supporting arguments for the relevance of SAED to study KBi_{10} structure are presented.

4.1. Structure model for KBi_{10} sample

4.1.1. Chemical composition of KBi_{10} layers and layer symmetry

One of the major differences between KBi_8 and KBi_{10} is their layer symmetry, as reflected by their *a*/*b* ratios ($1.732 = \sqrt{3}$ and $1.811 = \sqrt{3.28}$, respectively) [67]. Drits et al. showed that the symmetry of the phyllomanganate layers departs from being hexagonal when Mn^{3+} and Mn^{4+} cations are orderly distributed in rows parallel to the **b** axis, Jahn–Teller distorted Mn^{3+} octahedra being systematically elongated along the **a** axis (cooperative Jahn–Teller effect) [46]. The ordering of heterovalent Mn cations in birnessite layers is energetically favorable as it minimizes the steric strain induced by the presence of high amounts of distorted Mn^{3+} octahedra. In this case, the unit-cell *b* dimension (2.84–2.86 Å) is not significantly modified because the *b* direction is perpendicular to the direction of elongation of the Mn^{3+} octahedra and the Mn^{4+}–O and the four equatorial Mn^{3+}–O distances are equivalent. In contrast, the unit-cell *a* dimension is increased and, consequently, the *a*/*b* ratio varies as a function of the Mn^{3+}/Mn^{4+} ratio in the octahedral layer. For example, in crednerite ($CuMnO_2$) $a/b = 1.936$ ($Mn^{3+} = 100$ %) [85], in Na-rich buserite $a/b = 1.835$ ($Mn^{3+} = 33$ %) [70], in Na-rich birnessite $a/b = 1.817$ ($Mn^{3+} = 31$ %) [5,8,46], and in Ca-rich birnessite $a/b = 1.808$ ($Mn^{3+} = 22\%$) [70]. Thus, the *a*/*b* ratio is an indicator of the unique orientation of the elongated Mn^{3+} octahedra (cooperative Jahn–Teller effect) sensitive to the Mn^{3+}/Mn_{total} ratio in the layer when Mn^{3+} cations are ordered in rows. Note that in lithiophorite $[(Al^{3+}_{0.67}Li^{+}_{0.32})(Mn^{4+}_{0.68}Mn^{3+}_{0.32})O_2(OH)_2]$, which contains 32% of layer Mn^{3+}, the hexagonal symmetry of the layer is preserved ($a/b = \sqrt{3}$) because the Mn^{3+} octahedra are elongated along three directions in the **ab** plane [83]. Thus, both the *a* and *b* dimensions are enlarged relative to Mn^{3+}-free layers ($b = 2.925$ Å vs. 2.842–2.850 Å) [93].

KBi_{10} provides new evidence for the relationship between the *a*/*b* and the Mn^{3+}/Mn_{total} ratios when the layer symmetry is orthogonal, as both its *a*/*b* ratio (1.811) and chemical analysis indicate that it contains less Mn^{3+} than NaBi (0.25 vs. 0.31) and that they are ordered and systematically elongated along one direction. This finding is supported also by the shallowness of the "dunce's cap" feature at ~8 $Å^{-1}$ and the lower frequency of the EXAFS spectrum for KBi_{10} compared to NaBi (Fig. 6A). Lanson et al. showed that the amount of layer Mn^{3+} could be estimated from the ⟨Mn–O⟩ distance, taking as end-members $\langle d(Mn^{3+}\text{–}O)\rangle = 2.04$ Å, as calculated from crednerite and Mn oxyhydroxides, and $\langle d(Mn^{4+}\text{–}O)\rangle = 1.912$ Å, as calculated for λ–MnO_2 and hydrothermal birnessite (KBi_{hydr}) [8,76,77,85,94]. The ⟨Mn–O⟩ distance calculated for the $(Mn^{4+}_{0.75}Mn^{3+}_{0.25})$ layer cation composition of KBi_{10} (1.950 Å) is close to the experimental value (1.949 Å – Table 4). Similarly, the long Mn–O distance calculated as the weighted sum of the Mn^{4+}–O distance (1.912 Å in λ–MnO_2) and of the long Mn^{3+}–O distance (2.26 Å in credenerite) is 1.999 Å, and agrees with the XRD value (2.021 Å – Table 4).

4.1.2. Chemical composition of KBi_{10} layers and origin of the layer charge

Another important difference between KBi_8 and KBi_{10} is the origin of their layer charge. KBi_8 has a layer charge, which arises uniquely from cationic vacancies since the layer has no Mn^{3+} cations. This charge is compensated for by the binding of $Mn^{3+}_{interlayer}$ at vacancy sites and the sorption of K^+ [67]. In contrast, the layer charge deficit in KBi_{10} arises mostly from the substitution of 0.25 Mn^{4+}_{layer} by the same mole fraction of Mn^{3+}_{layer} and is compensated by 0.31 K^+ in the interlayer. According to XRD, layers are almost vacancy free. Additional support for the absence of layer vacancies in KBi_{10} follows from EXAFS

results. Quantitative analysis of the double antinode at ~8 $Å^{-1}$ has shown that its unique "dunce's cap" shape resulted from multiple scattering paths of the photoelectron between four aligned Mn shells in the layer plane [83]. This high-order pair correlation, up to an effective radial distance of $\sim 2.90 \times 3 = 8.7$ Å, can only be observed if the three successive Mn positions around a central Mn site are filled.

4.2. Layer symmetry and orientation of Mn^{3+} octahedra in sample 350-KBi_{10}

Structure models of KBi_{10} at room temperature and at 350 °C differ by their layer symmetries and, consequently, by their unit-cell parameters and interatomic distances. The in-plane layer cell parameters for hexagonal 350-KBi_{10} ($b = 2.894$ Å – Table 1) are significantly higher than those for hexagonal (1*H* and 2*H*) birnessites (2.844–2.848 Å at room temperature) [58,67,80,95]. As a result, 350-KBi_{10} has a longer ⟨d(Mn–O)⟩ (1.956 Å – Table 4) than 1*H* and 2*H* birnessites at room temperature (~1.91 Å) but, for steric reasons, it still coincides with the average distance in KBi_{10} (1.949 Å – Table 4), since the two samples likely have the same Mn^{3+}/Mn_{total} ratio. The slight increase of the ⟨Mn–O⟩ distance (from 1.949 to 1.956 Å, for KBi_{10} and 350-KBi_{10}, respectively) is likely related to thermal expansion.

One likely explanation for the layer symmetry modification with thermal treatment is a change of the azimuthal orientation of the elongation axes of the Mn^{3+} octahedra. If these axes are oriented with equal probability at $\pm n120°$ (*n* integer) directions, the resulting layer symmetry is hexagonal. This configuration likely distorts locally the O_{layer} lattice, and may explain the instability of the O_{layer} position during the structure refinement of 350-KBi_{10}. Random orientation of Mn^{3+} octahedra induces unfavorable lattice strains that are likely compensated for by the thermal energy available at 350 °C. Such random distribution of Mn^{3+} octahedra azimuthal orientation induces a significant increase of the unit-cell *b* parameter as compared to that measured for vacancy-free layers or for layers with a unique orientation of the long Mn^{3+}–O bonds in the **ac** plane. As mentioned above, such large *b* unit-cell dimension was reported for lithiophorite ($b = 2.912$ Å) [93] whose layers have a preserved hexagonal symmetry due to the random orientation of the Mn^{3+} octahedra in the **ab** plane [83]. Consistently, the *b* parameter determined for 350-KBi_{10} is increased compared to KBi_{10} (2.895 and 2.846 Å, respectively). As described by Gaillot et al. for hydrothermal KBi samples [77], this abrupt increase with increasing temperature (Table 1) cannot result solely from thermal motion as the unit-cell dilatation usually depends linearly on the temperature if the structure is not modified. The 2*O*–to–2*H* transition with an increase of the *b* parameter (from 2.846 to 2.895 Å) observed above 150 °C can thus be considered as a direct evidence for the presence of a significant amount of Mn^{3+} octahedra in KBi_{10} layers and for their systematic elongation along the **a** axis at room temperature.

4.3. General relationship between layer symmetry and origin of the layer charge in birnessites

The comparison between structural features of KBi_8, KBi_{10} and 350-KBi_{10} can be extended to all birnessite varieties, allowing general relationships between layer symmetry, layer cation composition, ⟨Mn–O⟩ distance and the origin of the layer charge to be drawn. HBi, KBi_8, KBi_{hydr} are characterized by low amounts of Mn^{3+}_{layer}, high layer vacancy contents being responsible for the layer charge deficit. As a result, these species exhibit short ⟨Mn–O⟩ distances (1.91–1.92 Å) and hexagonal symmetry with small *b* unit-cell dimensions (2.84–2.85 Å). In contrast, NaBi and KBi_{10} layers are almost devoid of vacancy and the layer deficit arises essentially from the presence of layer Mn^{3+} cations (25–30%), whose presence induces a higher ⟨Mn–O⟩ distance (>1.94 Å). In the latter case Jahn–Teller distorted Mn^{3+} octahedra are ordered at room temperature and their systematic elongation along the **a** axis leads to an orthogonal layer symmetry. When temperature is increased up to 250–350 °C, the symmetry of these Mn^{3+}-rich layers becomes hexagonal because of the random orientation of elongated Mn^{3+} octahedra. In this case, ⟨Mn–O⟩ distance remains high (>1.94 Å) whereas the *b* unit-cell dimension is increased significantly (>2.86 Å). Similar structural features are observed at room temperature when Mn^{3+} octahedra are ordered along the three equivalent directions [1 0 0], [1 1 0] and [1 $\bar{1}$ 0] of the **ab** plane, as in lithiophorite.

This global multi-parameter relationship between layer cation composition, ⟨Mn–O⟩ distances, *b* parameter values and layer symmetry allows deducing fundamental crystal-structure information on the origin of the layer charge and on the location of Mn^{3+} cations, when present (within the octahedral layer or in the interlayer), even for poorly crystallized birnessite varieties. Such inference was recently demonstrated by Villalobos et al. for turbostratic birnessite samples and further discussed by Drits et al. [96,97].

4.4. Interlayer structure of KBi_{10}

In KBi_{10}, the cohesion between adjacent layers mainly results from the electrostatic interaction between the interlayer K^+ cations and O_{layer}, H-bonds between $H_2O_{interlayer}$ and O_{layer} providing additional ties between layers. K^+ cations occupy one of the three possible sites in the interlayer prisms (Fig. 4). In such position, four K–O_{layer} distances are shorter than the other two (~2.95 and ~3.28 Å, respectively – Table 4). A similar shift of the interlayer K^+ position was reported for KBi_8 and hydrothermal KBi_{hydr} birnessite varieties as resulting from the strong undersaturation of O_{layer} coordinated to only two Mn^{4+} [67,77]. In KBi_{10}, whose layers are essentially vacancy-free, the presence of Mn^{3+}_{layer} is responsible for the undersaturation of O_{layer}. When a O_{layer} is coordinated to three Mn^{4+} octahe-

dra, it ideally receives $0.667 \times 3 = 2$ valence units (v.u.) and is fully saturated. If this O_{layer} is coordinated to two Mn^{4+} and one Mn^{3+}, or to one Mn^{4+} and two Mn^{3+}, it becomes partially undersaturated, ideally receiving only $0.667 \times 2 + 0.500 = 1.833$ v.u. or $0.667 + 0.500 \times 2 = 1.667$ v.u., respectively. Therefore, a specific distribution of Mn^{4+} and Mn^{3+} cations within adjacent layers (Fig. 7), and the resulting distribution of O_{layer} with various degrees of undersaturation, may account for the shift of the K^+ cations within the interlayer prisms, so as to better achieve local charge compensation of most undersaturated O_{layer}.

As found for samples KBi_8 and KBi_{hydr}, $H_2O_{interlayer}$, which are located in the interlayer mid-plane, are slightly shifted in the **ab** plane from the prism's edges defined by O_{layer} from adjacent layers towards the nearest Mn_{layer} (Fig. 4B) [67,77]. However, in KBi_{10} $H_2O_{interlayer}$ are shifted only along the **a** axis, refined occupancy of equivalent sites being nil. Resulting H_2O–O_{layer} distances and

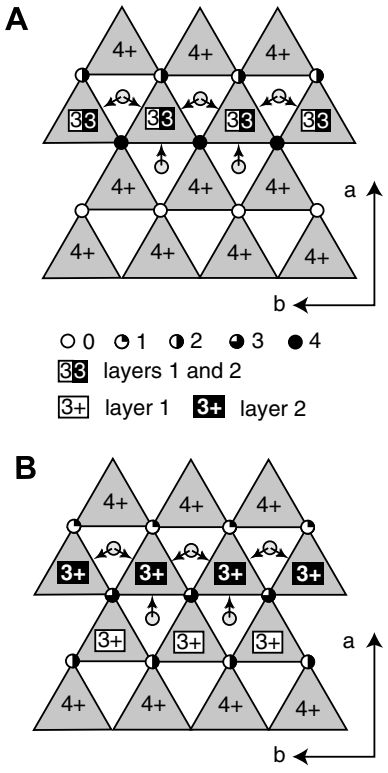

Fig. 7. Idealized distribution in projection on the **ab** plane of undersaturated O_{layer} within an interlayer region. 4+ represent Mn^{4+} cations located in the lower and/or in the upper octahedral layer. 3+ on black and white backgrounds represent Mn^{3+} cations located in the lower and upper octahedral layers, respectively. Circles represent O_{layer} from both the upper and lower surfaces of adjacent octahedral layers whose positions coincide in projection on the **ab** plane and define the edges of interlayer prisms. Different circle symbols are used to represent the degree of undersaturation of the O–O edge as a function of the total number of Mn^{3+}_{layer} coordinated to it (from 0 to 4 – See figure for equivalence). (A) Mn^{3+}-rich rows from adjacent layers coincide in projection on the **ab** plane. (B) Mn^{3+}-rich rows from adjacent layers do not coincide in projection on the **ab** plane (shift along the **a** axis).

O_{layer}–H_2O–O_{layer} angle, equal to 2.77 Å and 132.9°, respectively (Table 4), are typical for H-bonds.

4.5. Layer and interlayer structures of dehydrated samples KBi_{10}

When heated up to 350 °C sample KBi_{10} dehydrates, and the basal spacing is decreased from ~7.05 Å to ~6.39 Å (Table 1) due to the departure of $H_2O_{interlayer}$. Additional structural changes resulting from the heating include layer symmetry increase (*2O*–to–*2H* transition) as a result of the loss of cooperative Jahn–Teller effect. Despite the symmetry change and the partial interlayer collapse, position of interlayer K^+ cations is essentially unchanged. Such split of the K^+ site has been reported for hexagonal KBi structures (KBi_8 and KBi_{hydr}), both at room temperature and at 350 °C [67,77].

For sample Vacuum-KBi_{10}, the cooperative Jahn–Teller effect is preserved as no additional energy is available. Apart from the departure of $H_2O_{interlayer}$ and from the resulting interlayer collapse (from ~7.05 Å to ~6.47 Å), the structure of KBi_{10} and in particular its interlayer structure is maintained. K^+ cations occupy split positions similar to those in KBi_{10}, the sixfold coordination being provided by the nearest O_{layer} from adjacent layers with only limited migration of K^+ towards the center of the interlayer prism to allow for more appropriate K–O_{layer} distances. This similarity between hydrated and dehydrated interlayer structures of high-temperature KBi varieties thus allows using SAED to study the distribution of interlayer K^+ cations in dehydrated KBi_{10} structure, and extrapolating the obtained results to the hydrated structure. Results from such a study will be reported in the fourth paper of the series devoted to the study of high-temperature KBi varieties [66].

4.6. Origin of sample AfterT-KBi_{10} structural heterogeneity

The main difference between KBi_{10} specimens before and after the thermal treatment is a significant broadening, and weakening, of the *20l* reflections in sample After-KBi_{10} (Figs. 2 and 3). In addition, the fwhm of *20l* reflections of sample After-KBi_{10} decreases with increasing *l* index (solid circles – Fig. 3). These effects are similar to those described for heterogeneous KBi_{10h} birnessite [68]. Gaillot et al. demonstrated that these effects arise from the coexistence in the sample of several populations of particles which all have a *2O* structure but differ from each other by their unit-cell parameters that are related by Eq. 3 [68]. Two hypotheses were explored to account for this specific variation of the *a* and *b* parameters. First, local fluctuations of the redox conditions during cooling of sample 350-KBi_{10} may have led slightly different Mn^{3+} contents in individual crystals. This hypothesis is incompatible with the observed variation of the *a* and *b* unit-cell parameters, the *a*/*b* ratio determined for AfterT-KBi_{10} being slightly lower (1.805 Å) than that of KBi_{10}

(1.811 Å). If in both specimens layer Mn^{3+} octahedra were systematically elongated along the **a** axis, the *a* parameter decrease would then be related with the Mn^{3+}–to–Mn^{4+} oxidation during the thermal treatment. However, at 350 °C, reduction rather than oxidation was observed for hydrothermal KBi_{hydr} and pyrolusite (MnO_2) [68,77,98].

In the second hypothesis, the unit-cell dimension heterogeneity is related to contrasting orientation distribution of the long Mn^{3+}–O_{layer} bonds with respect to the **a** axis [77]. The maximum *a*/*b* ratio corresponds to KBi_{10} particles in which most Mn^{3+} octahedra are oriented with their long bonds along the **a** axis whereas in particles with lower *a*/*b* ratios the long Mn^{3+}–O bonds of some Mn^{3+} octahedra are oriented at ±120° with respect to the **a** axis. Such different azimuthal orientation distributions of Mn^{3+} octahedra likely originates from the cooling rate of 350-KBi_{10} which was too fast to allow a complete 2*H*–to–2*O* structure transformation. During this ''air quenching'' the random orientation of a small fraction of elongated Mn^{3+} octahedra was ''frozen'' in some KBi_{10} particles.

Acknowledgments

B.L. and V.A.D. acknowledge financial support from CNRS-PICS 709 program. V.A.D. acknowledges also the Russian Science Foundation and the Environmental Geochemistry Group (LGIT) for financial support. ACG thanks Jean-François Bérar (LdC, Grenoble) for technical assistance with his XND Rietveld refinement program. Martine Lanson and Delphine Tisserand (LGIT, Grenoble) and Céline Boissard (Hydr'ASA, Poitiers) are thanked for chemical and DT-TG analyses, respectively, and Matthew A. Marcus and Sirine Fakra for their assistance during measurements at the ALS. The ALS is supported by the Director, Office of Energy Research, Office of Basic Energy Sciences, Materials Sciences Division of the US Department of Energy, under Contract No. DE-AC02-05CH11231.

Appendix A. Supplementary data

Supplementary data associated with this article can be found, in the online version, at doi:10.1016/j.micromeso.2006.09.010.

References

[1] R. Giovanoli, E. Stähli, W. Feitknecht, Helv. Chim. Acta 53 (1970) 209.
[2] R. Giovanoli, E. Stähli, W. Feitknecht, Helv. Chim. Acta 53 (1970) 453.
[3] R.G. Burns, V.M. Burns, Phil. Trans. Roy. Soc. London A 286 (1977) 283.
[4] F.V. Chukhrov, A.I. Gorschkov, E.S. Rudnitskaya, A.V. Sivtsov, Izv. Akad. Nauk Geol. 9 (1978) 67.
[5] J.E. Post, D.R. Veblen, Amer. Mineral. 75 (1990) 477.
[6] A. Manceau, A.I. Gorshkov, V.A. Drits, Amer. Mineral. 77 (1992) 1133.
[7] A. Manceau, A.I. Gorshkov, V.A. Drits, Amer. Mineral. 77 (1992) 1144.
[8] B. Lanson, V.A. Drits, Q. Feng, A. Manceau, Amer. Mineral. 87 (2002) 1662.
[9] S.L. Suib, Curr. Opin. Solid State Mat. Sci. 3 (1998) 63.
[10] S. Ching, E.J. Welch, S.M. Hughes, A.B.F. Bahadoor, S.L. Suib, Chem. Mater. 14 (2002) 1292.
[11] P. Bezdicka, T. Grygar, B. Klapste, J. Vondrak, Electrochim. Acta 45 (1999) 913.
[12] Z.H. Liu, X.J. Yang, K. Ooi, J. Colloid Interface Sci. 265 (2003) 115.
[13] D.J. Jones, E. Wortham, J. Roziere, F. Favier, J.L. Pascal, L. Monconduit, J. Phys. Chem. Solids 65 (2004) 235.
[14] E. Wortham, B. Bonnet, D.J. Jones, J. Roziere, G.R. Burns, J. Mater. Chem. 14 (2004) 121.
[15] H. Kawaoka, M. Hibino, H. Zhou, I. Honma, Solid State Ionics 176 (2005) 621.
[16] M. Nakayama, S. Konishi, H. Tagashira, K. Ogura, Langmuir 21 (2005) 354.
[17] M. Nakayama, H. Tagashira, Langmuir 22 (2006) 3864.
[18] S.T. Wong, S. Cheng, C.S., Inorg. Chem. 31 (1992) 1165.
[19] S.T. Wong, S. Cheng, C.S., J. of the Chinese Chemical Society 40 (1993) 509.
[20] V. Ramamoorthy, A. Ramasubbu, S. Muthusubramanian, S. Sivasubramanian, Syn. Commun. 29 (1999) 21.
[21] Z.H. Liu, X.H. Tang, C.X. Zhang, Q. Zhou, Chem. Lett. 34 (2005) 1312.
[22] Z.M. Wang, Z. Liu, N. Yamashita, H. Kanoh, K. Ooi, Langmuir 18 (2002) 1957.
[23] Z.H. Liu, K. Ooi, H. Kanoh, W.P. Tang, T. Tomida, Chem. Lett. (2000) 390.
[24] Z.H. Liu, K. Ooi, H. Kanoh, W.P. Tang, X.J. Yang, T. Tomida, Chem. Mater. 13 (2001) 473.
[25] Y.F. Shen, R.P. Zerger, S.L. Suib, L. McCurdy, D.I. Potter, C.L. O'Young, J. Chem. Soc., Chem. Commun. (1992) 1213.
[26] Y.F. Shen, R.P. Zerger, R.N. DeGuzman, S.L. Suib, L. McCurdy, D.I. Potter, C.L. O'Young, Science 260 (1993) 511.
[27] Y.F. Shen, S.L. Suib, C.L. O'Young, J. Am. Chem. Soc. 116 (1994) 11020.
[28] Y.F. Shen, S.L. Suib, C.L. O'Young, J. Catal. 161 (1996) 115.
[29] Q. Feng, K. Yanagisawa, N. Yamasaki, Chem. Commun. (1996) 1607.
[30] Q. Feng, K. Yanagisawa, N. Yamasaki, J. Porous Mater. 5 (1998) 153.
[31] S.L. Brock, N.G. Duan, Z.R. Tian, O. Giraldo, H. Zhou, S.L. Suib, Chem. Mater. 10 (1998) 2619.
[32] Q. Feng, H. Kanoh, K. Ooi, J. Mater. Chem. 9 (1999) 319.
[33] S. Ching, K.S. Krukowska, S.L. Suib, Inorg. Chim. Acta 294 (1999) 123.
[34] Z.H. Liu, K. Ooi, Chem. Mater. 15 (2003) 3696.
[35] Q. Feng, J. Mater. Sci. Lett. 22 (2003) 999.
[36] X.H. Feng, F. Liu, W.F. Tan, X.W. Liu, H.Q. Hu, Science in China Series D Earth Sciences 47 (2004) 760.
[37] X.H. Feng, W.F. Tan, F. Liu, J.B. Wang, H.D. Ruan, Chem. Mater. 16 (2004) 4330.
[38] F.A. Al Sagheer, M.I. Zaki, Micropor. Mesopor. Mater. 67 (2004) 43.
[39] K.A. Malinger, K. Laubernds, Y.C. Son, S.L. Suib, Chem. Mater. 16 (2004) 4296.
[40] X.F. Shen, Y.S. Ding, J. Liu, K. Laubernds, R.P. Zerger, M. Polverejan, Y.C. Son, M. Aindow, S.L. Suib, Chem. Mater. 16 (2004) 5327.
[41] X.F. Shen, Y.S. Ding, J. Liu, J. Cai, K. Laubernds, R.P. Zerger, A. Vasiliev, M. Aindow, S.L. Suib, Adv. Mater. 17 (2005) 805.
[42] Z.H. Liu, L.P. Kang, K. Ooi, Y. Makita, Q. Feng, J. Colloid Interface Sci. 285 (2005) 239.
[43] L.Z. Wang, Y. Ebina, K. Takada, T. Sasaki, Chem. Commun. (2004) 1074.
[44] E. Paterson, R. Swaffield, L. Clark, Clay Miner. 29 (1994) 215.

[45] P. Le Goff, N. Baffier, S. Bach, J.-P. Pereira-Ramos, Mat. Res. Bull. 31 (1996) 63.
[46] V.A. Drits, E.J. Silvester, A.I. Gorshkov, A. Manceau, Amer. Miner. 82 (1997) 946.
[47] E.J. Silvester, A. Manceau, V.A. Drits, Amer. Miner. 82 (1997) 962.
[48] A. Manceau, B. Lanson, M.L. Schlegel, J.-C. Harge, M. Musso, L. Eybert Berard, J.-L. Hazemann, D. Chateigner, G.M. Lamble, Amer. J. Sci. 300 (2000) 289.
[49] A. Manceau, N. Tamura, R.S. Celestre, A.A. MacDowell, N. Geoffroy, G. Sposito, H.A. Padmore, Environ. Sci. Technol. 37 (2003) 75.
[50] D.C. Golden, J.B. Dixon, C.C. Chen, Clays & Clay Miner. 34 (1986) 511.
[51] R.M. Cornell, R. Giovanoli, Clays & Clay Miner. 36 (1988) 249.
[52] S.H. Kim, W.M. Im, J.K. Hong, S.M. Oh, J. Electrochem. Soc. 147 (2000) 413.
[53] W. Buser, P. Graf, W. Feitkneicht, Helv. Chem. Scripta 37 (1954) 2322.
[54] R.M. McKenzie, Miner. Mag. 38 (1971) 493.
[55] H.F. Herbstein, G. Ron, A. Weissman, J. Chem. Soc. (A) (1971) 1821.
[56] S. Ching, J.A. Landrigan, M.L. Jorgensen, N. Duan, S.L. Suib, C.L. O'Young, Chem. Mater. 7 (1995) 1604.
[57] R.J. Chen, P. Zavalij, M.S. Whittingham, Chem. Mater. 8 (1996) 1275.
[58] S.H. Kim, S.J. Kim, S.M. Oh, Chem. Mater. 11 (1999) 557.
[59] Y.U. Jeong, A. Manthiram, J. Solid State Chem. 156 (2001) 331.
[60] K. Kuma, A. Usui, W. Paplawsky, B. Gedulin, G. Arrhenius, Miner. Mag. 58 (1994) 425.
[61] Y. Ma, J. Luo, S.L. Suib, Chem. Mater. 11 (1999) 1972.
[62] R.J. Chen, T. Chirayil, P. Zavalij, M.S. Whittingham, Solid State Ionics 86–88 (1996) 1.
[63] S. Ching, J.L. Roark, N. Duan, S.L. Suib, Chem. Mater. 9 (1997) 750.
[64] S. Ching, D.J. Petrovay, M.L. Jorgensen, S.L. Suib, Inorg. Chem. 36 (1997) 883.
[65] S. Ching, S.L. Suib, Comment Inorganic Chem. 19 (1997) 263.
[66] A.-C. Gaillot, V.A. Drits, B. Lanson, Micropor. Mesopor. Mater., in preparation.
[67] A.-C. Gaillot, D. Flot, V.A. Drits, A. Manceau, M. Burghammer, B. Lanson, Chem. Mater. 15 (2003) 4666.
[68] A.-C. Gaillot, V.A. Drits, A. Plancon, B. Lanson, Chem. Mater. 16 (2004) 1890.
[69] V.A. Drits, Electron diffraction and high-resolution electron microscopy of mineral structures, Springer Verlag, Berlin Heidelberg, 1987, p. 304.
[70] V.A. Drits, B. Lanson, A.I. Gorshkov, A. Manceau, Amer. Mineral. 83 (1998) 97.
[71] V.A. Drits, B. Lanson, C. Bougerol Chaillout, A.I. Gorshkov, A. Manceau, Amer. Mineral. 87 (2002) 1646.
[72] K.J. Vetter, N. Jaeger, Electrochim. Acta 11 (1966) 401.
[73] J.J. Lingane, R. Karplus, Ind. Eng. Chem. Anal. Ed. 18 (1946) 191.
[74] J.-F. Bérar, G. Baldinozzi, CPD Newsletter 20 (1998) 3.
[75] A.L. Ankudinov, J.J. Rehr, Physical Review B 56 (1997) R1712.
[76] M.M. Thackeray, A. de Kock, W.I.F. David, Mat. Res. Bull. 28 (1993) 1041.
[77] A.-C. Gaillot, B. Lanson, V.A. Drits, Chem. Mater. 17 (2005) 2959.
[78] H.P. Klug, L.E. Alexander, X-ray diffraction procedures for polycrystalline and amorphous materials, Wiley, New York, 1974, p. 966.
[79] B. Lanson, V.A. Drits, A.-C. Gaillot, E. Silvester, A. Plancon, A. Manceau, Amer. Mineral. 87 (2002) 1631.
[80] B. Lanson, V.A. Drits, E.J. Silvester, A. Manceau, Amer. Miner. 85 (2000) 826.
[81] M.A. Marcus, A. Manceau, M. Kersten, Geochim. Cosmochim. Acta 68 (2004) 3125.
[82] A. Manceau, M.A. Marcus, N. Tamura, O. Proux, N. Geoffroy, B. Lanson, Geochim. Cosmochim. Acta 68 (2004) 2467.
[83] A. Manceau, C. Tommaseo, S. Rihs, N. Geoffroy, D. Chateigner, M. Schlegel, D. Tisserand, M.A. Marcus, N. Tamura, Z.S. Chen, Geochim. Cosmochim. Acta 69 (2005) 4007.
[84] A. Manceau, V.A. Drits, E.J. Silvester, C. Bartoli, B. Lanson, Amer. Mineral. 82 (1997) 1150.
[85] J. Töpfer, M. Trari, P. Gravereau, J.P. Chaminade, J.P. Doumerc, Z. Kristallogr. 210 (1995) 184.
[86] R.D. Shannon, Acta Crystallogr. A32 (1976) 751.
[87] B.K. Teo, EXAFS: basic principles and data analysis, Springer-Verlag, Berlin, 1986, p 349.
[88] A.L. Foster, G.E. Brown, G.A. Parks, Geochim. Cosmochim. Acta 67 (2003) 1937.
[89] A. Jurgensen, J.R. Widmeyer, R.A. Gordon, L.I. Bendell Young, M.M. Moore, E.D. Crozier, Amer. Mineral. 89 (2004) 1110.
[90] S.M. Webb, B.M. Tebo, J.R. Bargar, Amer. Mineral. 90 (2005) 1342.
[91] M. Bellotto, B. Rebours, O. Clause, J. Lynch, D. Bazin, E. Elkaïm, J. Phys. Chem. 100 (1996) 8527.
[92] T. Ressler, S.L. Brock, J. Wong, S.L. Suib, J. Phys. Chem. B 103 (1999) 6407.
[93] J.E. Post, D.E. Appleman, Amer. Miner. 79 (1994) 370.
[94] R.D. Shannon, P.S. Gumeman, J. Chenavas, Amer. Miner. 60 (1975) 714.
[95] F.V. Chukhrov, B.A. Sakharov, A.I. Gorshkov, V.A. Drits, Y.P. Dikov, Int. Geol. Rev. 27 (1985) 1082.
[96] M. Villalobos, B. Lanson, A. Manceau, B. Toner, G. Sposito, Amer. Mineral. 91 (2006) 489.
[97] V.A. Drits, B. Lanson, A.-C. Gaillot, Amer. Mineral., accepted for publication.
[98] Z.L. Wang, J.S. Yin, Y.D. Jiang, Micron 31 (2000) 571.